

An energy minimization method for the correction of cupping artifacts in cone-beam CT

Shipeng Xie,^a Wenqin Zhuang,^a and Haibo Li

Nanjing University of Posts and Telecommunications, College of Telecommunications & Information Engineering, Nanjing, Jiangsu, China
xie@njupt.edu.cn

Received 25 August, 2015; accepted 16 February, 2016

The purpose of this study was to reduce cupping artifacts and improve quantitative accuracy of the images in cone-beam CT (CBCT). An energy minimization method (EMM) is proposed to reduce cupping artifacts in reconstructed image of the CBCT. The cupping artifacts are iteratively optimized by using efficient matrix computations, which are verified to be numerically stable by matrix analysis. Moreover, the energy in our formulation is convex in each of its variables, which brings the robustness of the proposed energy minimization algorithm. The cupping artifacts are estimated as a result of minimizing this energy. The results indicate that proposed algorithm is effective for reducing the cupping artifacts and preserving the quality of the reconstructed image. The proposed method focuses on the reconstructed image without requiring any additional physical equipment; it is easily implemented and provides cupping correction using a single scan acquisition. The experimental results demonstrate that this method can successfully reduce the magnitude of cupping artifacts. The correction algorithm reported here may improve the uniformity of the reconstructed images, thus assisting the development of perfect volume visualization and threshold-based visualization techniques for reconstructed images.

PACS number(s): 87.57.cp

Key words: scatter correction, cupping artifacts, cone-beam CT

I. INTRODUCTION

An X-ray system with a large-area detector, which is commonly used for cone-beam computed tomography (CBCT), is more susceptible to cupping artifacts generated by scatter and beam hardening. X-ray scatter may lead to cupping artifacts, which is one of the most challenging problems in CBCT. Many correction methods that have been developed to reduce the cupping artifacts focus on reducing the scattered photons on the projective image. One such hardware-based method involves physical scatter rejection techniques in the data acquisition system, such as the use of an air gap,⁽¹⁾ antiscatter grid,⁽²⁾ or bowtie filter.⁽³⁾ The second category of software-based approaches are based on Monte Carlo simulation,^(4,5,4) which use Monte Carlo (MC) simulations to model the scatter distribution by tracing the history of photons from the source to the detector. Some improved Monte Carlo simulation algorithms, such as the GPU-based method,^(6,7) the combination of several variance-reduction techniques,⁽⁸⁾ and the model-based volume restoration approach,⁽⁹⁾ have been proposed in recent years. However, even using the fast algorithm, the formidably heavy computation load associated with Monte Carlo scatter estimation hinders its real-life applications. The third category of methods estimates the contribution

^a Corresponding co-authors: Shipeng Xie and Wenqin Zhuang, Nanjing University of Posts and Telecommunications, College of Telecommunications & Information Engineering, Nanjing, Jiangsu, China 210003; phone: (+86) 15951939322; fax: (+86)02583492420; emails: xie@njupt.edu.cn and zhuangwq@njupt.edu.cn

of scatter in the measured projection data and then subtracts it from the measured projection data, such as the beam-stop array method,⁽¹⁰⁾ the moving blocker method,⁽¹¹⁾ primary modulation,^(12,13,14) artifact-suppressed dictionary learning method,^(15,16) and others.^(17,18) However, these types of correction methods add extra hardware to the CBCT system, which can add difficulty and complexity. Although the image correction approach cannot be used to recover the contrast sensitivity, it is effective in recovering the accuracy of the projection image data for X-ray transmission measurement and in reducing the nonuniformity of the CBCT signals that may be depicted as the cupping artifacts. All of these methods act directly on the projective image, requiring correction of every projected image. However, scatter correction performed on the projection images requires extensive computation to estimate the two-dimensional scatter signal profile in conjunction with the use of sampled physical scatter measurements that are integrated with the image acquisition process or performed with additional exposures. We had observed that cupping artifacts can be corrected by using reconstructed image. Similar observations had also been reported in the literature.^(19,20)

In this study, we investigated an energy minimization method for cupping artifacts correction in the reconstructed image of CBCT. As we know, the cupping artifacts in reconstructed images are slow nonlinear varying. The reconstructed images can be decomposed into two parts: primary images and cupping artifacts images. To correct the cupping artifacts, we adapted a bias correction method previously developed for MR images.⁽²¹⁾ The robustness of the proposed algorithms was demonstrated in phantoms. This correction algorithm reported here can improve the uniformity of the reconstructed images, thus assisting the development of perfect volume visualization and threshold-based visualization techniques for the reconstructed images.

II. MATERIALS AND METHODS

A. Decomposition of reconstructed image

Reconstruction images based on the work by Feldkamp et al.⁽²²⁾ are popular in CBCT. The reconstruction image set can be equivalently written as

$$f = \frac{1}{4\pi} \int_0^{2\pi} \frac{d_{so}^2}{d_{so} + r \cdot s} \int_{-\infty}^{\infty} \frac{d_{so}}{d_{so}^2 + t^2 + z^2} \cdot I_{3D}(t, z(r), \phi) \cdot \int_{-\infty}^{\infty} |\omega| e^{j2\pi\omega(t(r)-1)} d\omega dt d\phi \quad (1)$$

where d_{so} is the distance of the source-to-rotation axis, the coordinate along the detector that specifies the point of detection is (t, z) , $I_{3D}(t, z(r), \phi)$ is the sequence of the projected image, r is extend from the origin to the reconstruction point, s is a unit vector along the ray from the source to the axis of rotation (i.e., normal to the detector), $z(r) = \frac{d_{so}(r \cdot z)}{d_{so} + r \cdot s}$, and $\int_{-\infty}^{\infty} |\omega| e^{j2\pi\omega(t(r)-1)} d\omega$ is the convolution function.

To address cupping artifacts in the reconstructed image, we formulate our method based on an image model that describes the composition of projected images, which are affected by scatter and beam hardening. A projected image can be modeled as

$$I_{3D} = P_{3D} + S_{3D} + n \quad (2)$$

where P_{3D} is the image derived from primary photons, S_{3D} is the component caused by scatter and beam hardening, and n is additive noise with zero-mean. The P_{3D} measures an intrinsic physical property of the objects being imaged, which is therefore assumed to be piecewise

(approximately) constant. We can prove that the reconstructed images based on the Feldkamp study⁽²²⁾ can be written as follows:

$$f = f_p + f_s + f_n \quad (3)$$

where f_p , f_s and f_n are produced by P_{3D} , S_{3D} , and noise n .

As in Eq. (2), a reconstruction image can be described as the true image plus the cupping artifacts. In the following section, we will give a method to remove from the reconstructed images.

B. Representations of intrinsic components

To effectively use the properties of the f_s and f_p , the f_s is represented by a linear combination of a given set of smooth basis function g_1, \dots, g_M , which ensures the smoothly varying property of the cupping artifacts. The estimation of the scatter field is performed by finding the optimal coefficients w_1, \dots, w_M in the linear combination $f_s(x) = \sum_{k=1}^M w_k g_k$. Consequently, the $f_s(x)$ can be expressed in the following vector form: $f_s(x) = w^T G(x)$, where $G(x) = (g_1(x), \dots, g_M(x))^T$. In this paper, we use 10 polynomials as the smooth scatter function.

We presume that there are N types of tissues in the image domain Ω_i . The true image $f_p(x)$ is virtually a constant c_i for x in the i -th tissue. We denote that the i -th tissue is located in the region Ω_i . Each Ω_i can be represented by its membership function u_i . In ideal conditions, the membership function u_i is a binary membership function, with $u_i(x) = 1$ for $x \in \Omega_i$ and $u_i(x) = 0$ for $x \notin \Omega_i$. Given the membership functions u_i and constant c_i , the image f_p can be expressed by

$$f_p = \sum_{i=1}^N c_i u_i(x) \quad (4)$$

C. Energy formulation for component optimization

We propose an energy minimization formulation previously developed for MR images. In this model, we take into account the problem of finding f_s and f_p of an observed postreconstructed image f such that the following energy is minimized

$$F(f_s, f_p) = \int_{\Omega} |f(x) - f_p(x) - f_s(x)|^2 dx \quad (5)$$

Clearly, if there are no constraints on the variables f_s and f_p , minimization of F is an ill-posed problem. Actually, the energy $F(f_s, f_p)$ is minimized by any variables f_s and $f_p = f - f_s$ which are described in the Materials & Methods section B above. With these representations of the true image and the cupping artifacts, the energy $F(f_s, f_p)$ can be expressed as follow:

$$F(f_s, f_p) = F(u, c, w) = \int_{\Omega} \left| f(x) - \sum_{i=1}^N c_i u_i(x) - w^T G(x) \right|^2 dx \quad (6)$$

D. Optimization of the cupping artifacts

A desirable property of this energy $F(u, c, w)$ is that each variable, u , c , or w is convex. This property insures that $F(u, c, w)$ has a unique minimum point in each of its variables.

For fixed c and u , we can minimize $F(u, c, w)$. This can be achieved by solving the equation $\frac{\partial F}{\partial w} = 0$. It can be shown that

$$\frac{\partial F}{\partial w} = -2 \int_{\Omega} G(x) \left| f(x) - \sum_{i=1}^N (c_i u_i(x)) \right| dx + 2w \int_{\Omega} G(x) G(x)^T dx = 0 \quad (7)$$

The equation can be expressed as follow:

$$Aw = v \quad (8)$$

where $A = \int_{\Omega} G(x) G(x)^T dx$, $v = \int_{\Omega} G(x) \left| f(x) - \sum_{i=1}^N (c_i u_i(x)) \right| dx$.

It is easy to show that the matrix A is nonsingular.⁽²¹⁾ Consequently, the vector \hat{w} can be expressed as:

$$\hat{w} = A^{-1}v \quad (9)$$

The estimated bias field is computed by

$$\hat{f}_s = \hat{w}^T G(x) \quad (10)$$

For fixed w and u , the $F(u, c, w)$ can be minimized with the variable $c = \hat{\hat{c}} = (c_1, \mathbf{L}, c_N)^T$.

$$\hat{\hat{c}}_i = \frac{\int_{\Omega} (f(x) - \hat{f}_s(x)) u_i(x) dx}{\int_{\Omega} u_i^2(x) dx}, \quad i = 1, \mathbf{L}, N \quad (11)$$

It can be shown that $\hat{\hat{u}} = (u_1, \mathbf{L}, u_N)^T$ is given by

$$\hat{\hat{u}}_i = \begin{cases} 1, & i = i_{\min}(x) \\ 0, & i \neq i_{\min}(x) \end{cases} \quad (12)$$

where $i_{\min}(x) = \arg \min \{f(x) - c_i - w^T G(x)\}$.

E. Implementation

From the previous sections, we summarize the scheme of minimization of the energy $F(u, c, w)$ as shown in Fig. 1.

$|c^{(n)} - c^{(n-1)}| < \varepsilon$ is the convergence criterion, where $c^{(n)}$ is updated from the vector c at the n -th iteration, and ε is assigned to 0.001. The $F(u, c, w)$ rapidly declines and meets the minimum value in less than 15 iterations in our applications.

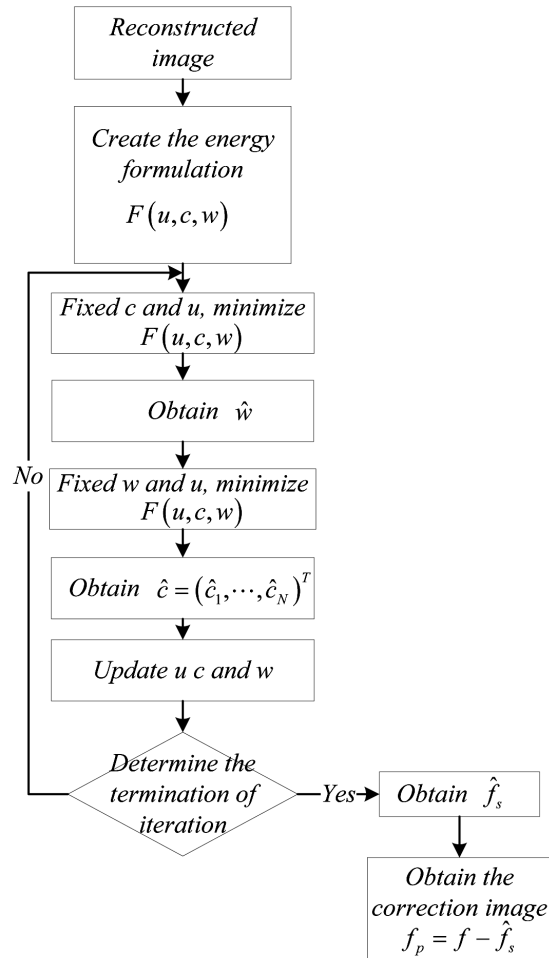


FIG. 1. The process of the proposed cupping artifacts correction.

F. Evaluation of cupping correction

Quantitative image quality parameters were analyzed according to the work by Jo et al.⁽¹⁴⁾ The magnitude of cupping $\tau_{\text{cup}} = 100(u_{M,\text{edge}} - u_{M,\text{center}})/u_{M,\text{edge}}$ was extracted in terms of voxel values at the center $u_{M,\text{center}}$ and edge $u_{M,\text{edge}}$ of the water phantom.

Root mean square contrast (RMSC) is defined as the standard deviation of the pixel intensities:

$$RMSC = \sqrt{\frac{1}{MN} \sum_{i=0}^{N-1} \sum_{j=0}^{M-1} (I_{ij} - \bar{I})^2} \quad (13)$$

where I_{ij} is the i -th j -th element of the two-dimensional image of size M by N and \bar{I} is the average intensity of all pixel values in the image. The image I is assumed to have its pixel intensity normalized in the range $[0,255]$.

III. RESULTS

A. Skull phantom

The experimental data were obtained from Rezvani et al.⁽²³⁾ The image size is 211×211 . After correction, the images presented significantly improved signal uniformity, as shown in Fig. 2 and Fig. 3. For a quantitative analysis of the reconstructed images, we measure the magnitude

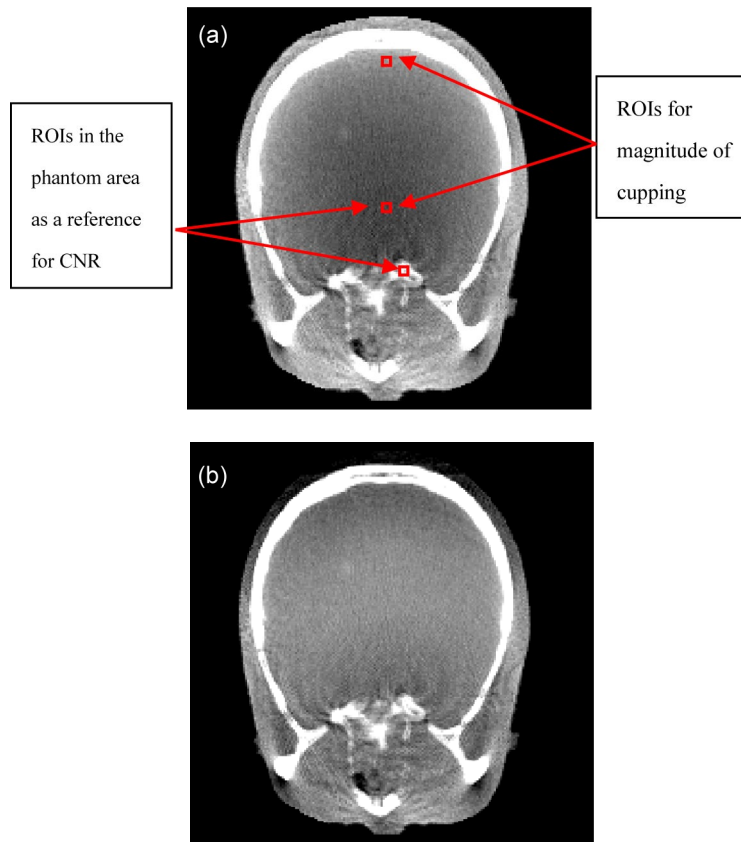


FIG. 2. Sample axial views selected from reconstructed images of the skull phantom before (a) and after cupping artifact correction (b).

of cupping in the selected ROIs, as shown in Fig. 2(a). The analyses are given in Table 1. The correction process take 1.89 s for a slice (CPU: i5-2450, RAM: 6GB, GPU: NVIDIA GeForce 610M).

The 1D horizontal profile before and after correction can be seen in Fig. 3. As before, a great reduction in the cupping artifact is observed in the corrected image.

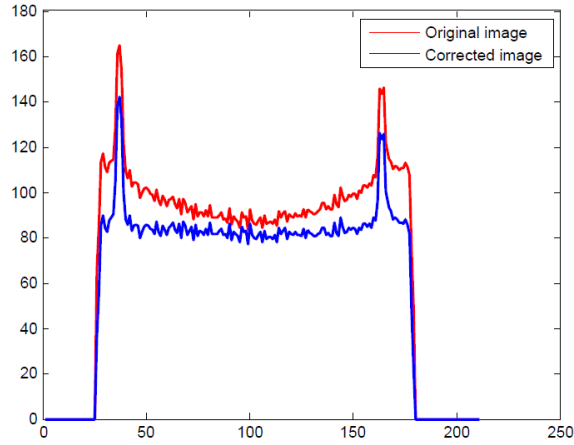


FIG. 3. The 1D horizontal profile of the measured skull phantom: The column is the profiles of the images, which are at middle row in Fig. 2.

TABLE 1. Quantitative analysis of a skull phantom. Reconstructed image before correction of cupping artifacts (RI_BC), reconstructed image after correction of cupping artifacts (RI_AC).

	$RMSE$ (<i>edge</i>)	$RMSE$ (<i>center</i>)	τ_{cup} (%)	CNR
RI_BC	2.22	1.89	16.44	5.61
RI_AC	2.26	1.68	8.9	9.52

B. CTP486 phantoms

CTP486 (The Phantom Laboratory, Salem, NY) is used in this experiment. Figure 4 shows the reconstructed images. The CTP486 module is cast from a uniform material that has a CT number within 2% (0-20H) of water. The image size is 229×229 . The correction process take 1.93 s for a slice (CPU: i5-2450, RAM: 6GB, GPU: NVIDIA GeForce 610M).

ROIs for magnitude of cupping are shown in Fig. 4(a). Our approach clearly reduces the τ_{cup} magnitude by an average of 95%.

The 1D horizontal profile before and after correction can be observed in Fig. 5.

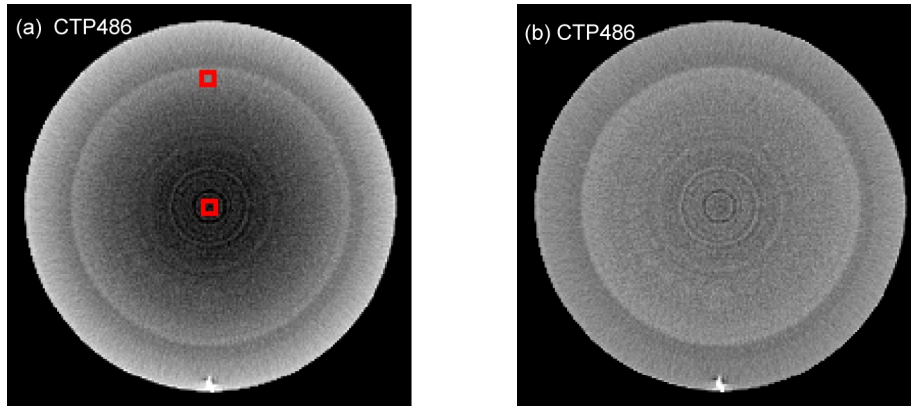


FIG. 4. Sample axial views selected from two different slices of reconstructive images of the CTP486 in the CatPhan500 are shown before (a) and after scatter correction (b). The images are rescaled to the same size such that they can be displayed in the same figure and are displayed at the same gray scale. ROIs for magnitude of cupping are marked with red blocks.

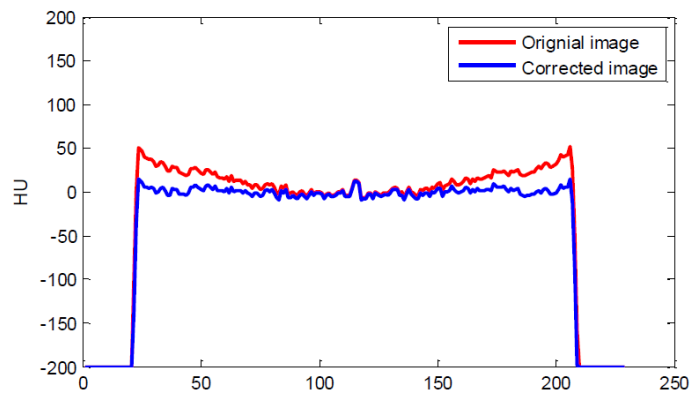


FIG. 5. The 1D horizontal profile of the measured phantom. The column is the profiles of the images, which are at middle row in Fig. 4.

C. A mouse bone

A mouse's bone scan data are obtained from a Micro-CT called Hiscan-M1000 (Hays Feder Information Technology Co., Suzhou, China). The acquisitions for the reconstructed images consist of 360 projections, with 80 kVp, 200 μ A, 30 ms. Sample axial views selected from the reconstructive images of the mouse bone is shown before (Fig. 6(a)) and after scatter correction (Fig. 6(b)). The image size is 339×339 . The correction process takes 2.7 s for a slice (CPU: i5-2450, RAM: 6GB, GPU: NVIDIA GeForce 610M). We measure the magnitude of cupping in the selected ROIs, as shown in Fig. 6(a). Our approach reduces the τ_{cup} from 23.8% to 9.8%. The quantitative image quality analyses are provided in Table 2.

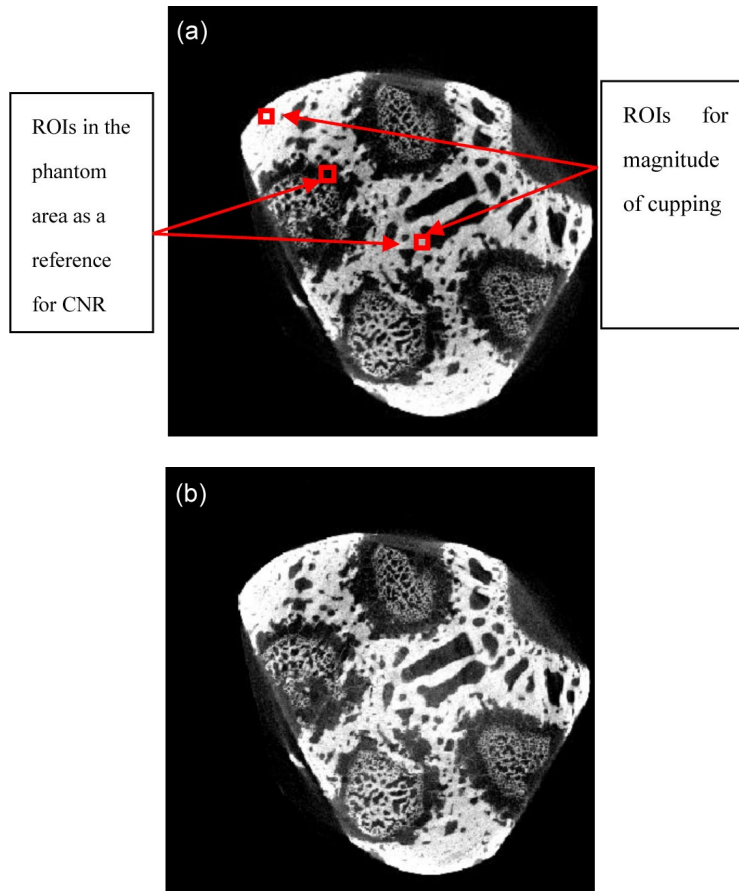


FIG. 6. Sample axial views selected from the reconstructive images of the mouse's bone are shown before (a) and after scatter correction (b).

TABLE 2. Quantitative analysis of a mouse bone. Reconstructed image before correction of cupping artifacts (RI_BC), reconstructed image after correction of cupping artifacts (RI_AC).

	<i>RMSE</i> (<i>edge</i>)	<i>RMSE</i> (<i>center</i>)	τ_{cup} (%)	<i>CNR</i>
RI_BC	6.36	3.57	28.8	11.97
RI_AC	6.49	3.57	9.8	15.87

D. Pelvis patient

The proposed correction method is further evaluated on the CBCT images acquired from a pelvis patient. The tabletop system operates in the full-fan scan mode and a data acquisition in a 360° scan. After correction, the images presented significantly improved signal uniformity, as shown in Fig. 7.

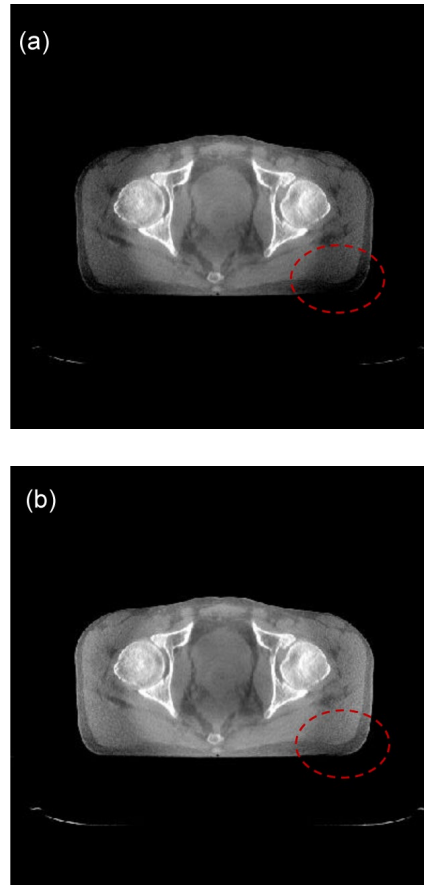


FIG. 7. Sample axial views selected from two different slices of the pelvis CBCT image are shown before (a) and after scatter correction (b). The images are displayed in the same window.

E. Comparison with another method

In this study, our idea is originated from MRI. We find another cupping artifact method inspired by the MR bias correction method from the work by Yang et al.⁽¹⁹⁾ The results are shown in Fig. 8. For a quantitative analysis of the reconstructed images, we measure the magnitude of cupping and CNR in the selected ROIs, and the quantitative analyses are given in Table 3.

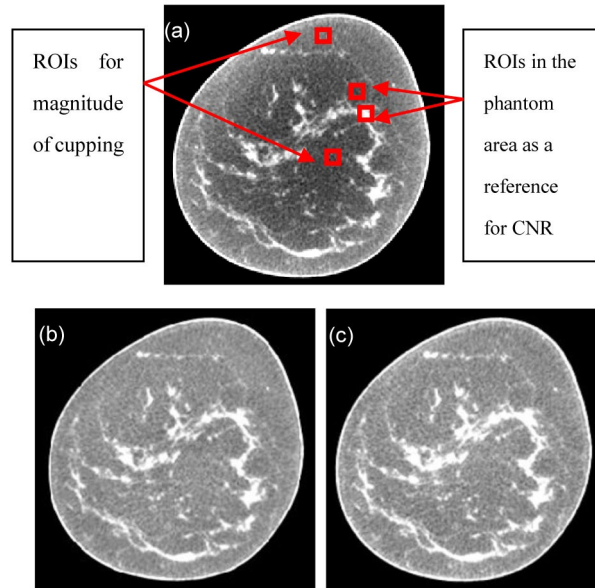


FIG. 8. Comparison of breast CT images before (bottom left) and after (top) cupping artifact correction, using the method developed by Yang et al.⁽¹⁹⁾ (Bottom right) This paper's method.

TABLE 3. Reconstructed image before correction of cupping artifacts (RI_BC), reconstructed image after correction of cupping artifacts, from work by Yang et al.⁽¹⁹⁾ (RI_AC_Ref19), reconstructed image after correction of cupping artifacts using this method (RI_AC_our).

	<i>RMSE</i> (<i>edge</i>)	<i>RMSE</i> (<i>center</i>)	$\tau_{cup}^{(%)}$	<i>CNR</i>
RI_BC	4.42	5.37	22.27	11.48
RI_AC_Ref19	5.31	4.41	0.6	7.74
RI_AC_our	4.40	5.8	0.7	8.59

IV. DISCUSSION & CONCLUSIONS

For a quantitative analysis of the reconstructed images, we measure the magnitude of cupping in the selected ROIs for skull phantom, shown in Fig. 2. The analyses are given in Table 1. Our approach clearly reduces the τ_{cup} magnitude by an average of 50%. It can be seen that the proposed correction method works very well. As shown in Figs. 3 and 5 and Tables 1 and 2, the proposed method markedly reduced the magnitude of cupping, increased the CNR of CBCT, and demonstrated no obvious change of the RMSEs. In other words, the image quality was improved after cupping artifact correction.

Our approach clearly reduces the τ_{cup} magnitude by an average of 95% in the CTP486 phantom. As shown in Fig. 4, a marked reduction in cupping artifacts is observed in the corrected image.

As shown in Fig. 7, the proposed method can significantly improved signal uniformity and the image quality. The results clearly show that the proposed correction method works very well.

In Yang et al.,⁽¹⁹⁾ the method automatically corrects the cupping artifacts using a nonparametric coarse-to-fine approach which allows the cupping artifacts to be modeled with different frequency ranges and without user supervision. Figure 8 shows that our method equally for the correction of cupping artifacts, as well as that detailed in Yang et al. Our method has a higher average CNR of 8.59 (Fig. 8(c)), which is higher than the previously reported average CNR (Fig. 8(b)) by 1.11-fold.

In Reitz et al.,⁽²⁴⁾ a scatter correction method is based on a superposition of precalculated Monte Carlo generated pencil beam scatter kernels. The cupping artifacts of water phantom are reduced from 20% without scatter correction to 4% with scatter correction (reduces the τ_{cup} magnitude 80%). In our method, the cupping artifacts of CTP486 (water phantom) is reduced by about 95%.

As our correction method involves processing of the reconstructed images only, it does not require any hardware modifications for signal measurements. The correction algorithm reported here may improve the uniformity of the reconstructed images, thus assisting in the development of perfect volume visualization and image segmentation techniques.

ACKNOWLEDGMENTS

This work was supported by the National Natural Science Foundation of China (Grant No. 11547155 and No. 81530060), National Natural Science Foundation of Jiangsu Province (Grant No. BK20130883), the NUPTSF (Grant No. NY213011 and No. NY214026) and the National High-tech R&D Program for Young Scientists by the Ministry of Science and Technology of China (863 Program, Grant No. 2015AA020917).

COPYRIGHT

This work is licensed under a [Creative Commons Attribution 3.0 Unported License](https://creativecommons.org/licenses/by/3.0/).

REFERENCES

1. Rührnschopf EP and Klingenberg K. A general framework and review of scatter correction methods in cone beam CT, Part 2: scatter estimation approaches. *Med Phys.* 2011;38(9):5186–99.
2. Wiegert J, Bertram M, Schaefer D, et al. Performance of standard fluoroscopy antiscatter grids in flat-detector-based cone-beam CT. *Proc. SPIE: Medical Imaging 2004.*
3. Mail N, Moseley D, Siewerdsen J, Jaffray D. The influence of bowtie filtration on cone-beam CT image quality. *Med Phys.* 2009;36(1):22–32.
4. Selvam TP, Mishra S, Vishwakarma RS. Monte Carlo calculation of beam quality correction for solid-state detectors and phantom scatter correction at 137Cs energy. *J Appl Clin Med Phys.* 2014;15(1):4445.
5. Kim S, Song H, Samei E, Yin FF, Yoshizumi TT. Computed tomography dose index and dose length product for cone-beam CT: Monte Carlo simulations. *J Appl Clin Med Phys.* 2011;12(2):3395.
6. Sisniega A, Zbijewski W, Stayman J, et al. Ultra-fast Monte Carlo simulation for cone beam CT imaging of brain trauma [abstract]. *Med Phys.* 2014;41(6):542.
7. Gaens M, Bert J, Pietrzyk U, Autret A, Shah NJ, Visvikis D. GPU-accelerated Monte Carlo based scatter correction in brain PET/MR. *EJNMMI Phys.* 2014; 1(Suppl 1):A32.
8. Mainegra-Hing E and Kawrakow I. Fast Monte Carlo calculation of scatter corrections for CBCT images. *J Phys: Conference Series.* 2008;102(1):012–17.
9. Zhang G, Jacobs R, Bosmans H. A model-based volume restoration approach for Monte Carlo scatter correction in image reconstruction of cone beam CT with limited field of view. *Proc. SPIE: Medical Imaging 2013.*
10. Cai W, Ning R, Conover D. Simplified method of scatter correction using a beam-stop-array algorithm for cone-beam computed tomography breast imaging. *Optic Eng.* 2008;47(9):957–66.
11. Ouyang L, Song K, Wang J. A moving blocker system for cone-beam computed tomography scatter correction. *Med Phys.* 2013;40(7):071903.

12. Zhu L, Bennett NR, Fahrig R. Scatter correction method for X-ray CT using primary modulation: theory and preliminary results. *IEEE Trans Med Imaging*. 2006;25(12):1573–87.
13. Gao H, Fahrig R, Bennett NR, Sun M, Star-Lack J, Zhu L. Scatter correction method for x-ray CT using primary modulation: phantom studies. *Med Phys*. 2010;37(2):934–46.
14. Jo BD, Lee YJ, Kim DH, Jeon PH, Kim HJ. Scatter correction method with primary modulator for dual energy digital radiography: a preliminary study. *Proc. SPIE. Medical Imaging* 2014.
15. Chen Y, Shi L, Feng Q, et al. Artifact suppressed dictionary learning for low-dose CT image processing. *IEEE Trans Med Imaging*. 2014;33(12):2271–92.
16. Chen Y, Yang Z, Hu Y, et al. Thoracic low-dose CT image processing using an artifact suppressed large-scale nonlocal means. *Phys Med Biol*. 2012;57(9):2667–88.
17. Shipeng X, Limin L. Scatter correction for cone beam CT using self-adaptive scatter kernel superposition. *Chinese Physics C*. 2012;36(6):566–72.
18. Aubry JF, Cheung J, Morin O, Gottschalk A, Beaulieu L, Pouliot J. Correction of megavoltage cone-beam CT images of the pelvic region based on phantom measurements for dose calculation purposes. *J Appl Clin Med Phys*. 2009;10(1):33–42.
19. Yang X, Wu S, Sechopoulos I, Fei B. Cupping artifact correction and automated classification for high-resolution dedicated breast CT images. *Med Phys*. 2012;39(10):6397–406.
20. Xie S, Li C, Li H, Ge Q. A level set method for cupping artifact correction in cone-beam CT. *Med Phys*. 2015;42(8):4888–95.
21. Li C, Gore J C, Davatzikos C. Multiplicative intrinsic component optimization (MICO) for MRI bias field estimation and tissue segmentation. *Magn Reson Imaging*. 2014;32(7):913–23.
22. Feldkamp LA, Davis LC, Kress JW. Practical cone-beam algorithm. *JOSA A*. 1984;1(6):612–19.
23. Rezvani N, Aruliah D, Jackson K, Moseley D, Siewerdsen J. OSCaR: an open-source cone-beam CT reconstruction tool for imaging research [abstract] *Med Phys*. 2007;34(6):2341.
24. Reitz I, Hesse B M, Nill S, Tücking T, Oelfke U. Enhancement of image quality with a fast iterative scatter and beam hardening correction method for kV CBCT. *Z Med Phys*. 2009;19(3):158–72.